Petroleum Science 22 (2025) 1686–1698

Contents lists available at ScienceDirect

Petroleum Science

journal homepage: www.keaipublishing.com/en/journals/petroleum-science

Original Paper

Ball-sealer transport characteristics and plugging performance in vertical wells

Ying Liu [a], Hai Qu [a,*], Mao Sheng [b], Hai-Zhu Wang [b], Ting-Xue Jiang [c], Shi Wang [a]

[a] Chongqing University of Science and Technology, Chongqing, 401331, China
[b] China University of Petroleum, Beijing, 102249, China
[c] Sinopec Research Institute of Petroleum Engineering Technology Co., Ltd., Beijing, 100101, China

ARTICLE INFO

Article history:
Received 28 September 2024
Received in revised form
6 January 2025
Accepted 12 January 2025
Available online 13 January 2025

Edited by Yan-Hua Sun

Keywords:
Ball sealer
Hydraulic fracturing
Vertical wells
CFD-DEM

ABSTRACT

Ball-sealer plugging is a cost-effective method for hydraulic fracturing in vertical wells, yet the transport and plugging behavior of ball sealers remains poorly understood. This paper investigates ball-sealer plugging using both experimental and numerical approaches. A coupled computational fluid dynamics (CFD) and discrete element method (DEM) model simulates ball transport under field conditions, validated by experiments in inclined pipes. Results show that plugging performance improves with a higher flow rate ratio of the perforation, allowing effective plugging even when the ball is far from the target perforation. There exists a threshold distance between the ball and the perforation under specific conditions. The closer the ball is to the wellbore wall, the higher the likelihood of successful plugging. Low-density balls can enhance plugging performance to some extent. At high flow rates, ball inertia along the wellbore axis increases, reducing the ball's ability to redirect and weakening plugging performance. Ball interactions also affect their positioning and plugging success. In vertical wells with multiple clusters, prioritizing higher flow rates to the first fracturing cluster optimizes overall plugging performance and minimizes excessive plugging in lower, under-stimulated clusters. These findings offer valuable insights for optimizing ball-sealer deployment in well completions, improving operational outcomes.

1. Introduction

Vertical well with perforations is a primary completion strategy for hydrocarbon reservoirs with vertically stacked pay zones (Miskimins, 2019; Qu et al., 2024b; Wang et al., 2012). Hydraulic fracturing cooperates with ball sealers to stimulate multiple zones at a much lower cost than packer fracturing (Qu et al., 2024a; Tan et al., 2018). Balls temporarily plug some perforations to divert fracture fluid to under-stimulated zones (Bilden et al., 1998; Chen et al., 2023a; Liu et al., 2023). It is successfully applied in acid stimulation, matrix acidizing (Chen et al., 2024; Gabriel and Erbstoesser, 1984), and horizontal well fracturing (Yuan et al., 2022). However, applying ball sealers in vertically perforated wells introduces unique challenges. Numerous studies have shown that ball sealers often fail to achieve effective diversion (Cheng et al., 2021). In many cases, ball sealers do not plug the target perforation at the precise moment, and the wellhead pressure response is minimal when the ball reaches the intended location (Yuan et al., 2021). Due to the lack of in-depth understanding of the transport and plugging characteristics and the absence of clear guidelines, field operations often rely on the experience. It is necessary to understand ball transport behavior in vertical well with perforations.

Brown et al. (1963) proposed the equations of ball transport in a vertical well. Once the inertial force on the ball was greater than the drag force, the ball missed the perforations to the rathole. At best, it seated only the lowermost perforations. Erbstoesser (1980) conducted laboratory tests in a vertical pipe with side holes and found that buoyant balls had a larger plugging performance than non-buoyant balls. Field trials in Saudi Arabia confirm that buoyant ball sealers are the optimal solution for the matrix acidizing of perforated completions. Nozaki et al. (2013) experimented with ball plugging in a full-scale flow device to evaluate ball-sealer plugging performance. The ball-sealer densities ranged from 900 to 1190 kg/m^3. The maximum fluid velocity was 1.35 m/s. Due to gravity and hole azimuth, the ball-seating behavior varies significantly between vertical and horizontal wells. Buoyant and nonbuoyant balls had a statistical nature in perforation plugging. In a horizontal well,

* Corresponding author.
E-mail address: quhai729@163.com (H. Qu).

https://doi.org/10.1016/j.petsci.2025.01.002

the plugging rate reaches approximately 85% with a ball sealer-to-perforation ratio exceeding 2.5. Yuan et al. (2022) developed a large-scale experimental system with a diameter of 84 mm to test ball-sealer transport under high flow rates and pressures. Two types of diverter balls with densities of 1260 and 1100 kg/m^3 were used. The mean fluid velocity was up to 1.0 m/s. There are significant differences in diverter transport due to varying flow distribution among perforations. The ball can only enter a side hole as its flow rate reaches a specific threshold. High-viscous fluid can improve the plugging rate of high-side perforations. It is found that the perforation flow ratio has an "oblique L-shaped" relationship with the injection rate. However, during the pumping of balls, the flow rate ranges from 2 to 5 m^3/min (Miskimins, 2019), which is challenging to achieve in a laboratory device. Since the flow rate significantly affects the ball transport behavior, ball-sealer transport characteristics and plugging performance still need to be clarified, especially under field conditions.

Computational fluid dynamics (CFD) combined with the discrete element method (DEM) becomes an excellent solution that studies ball transport under high flow rate and pressure (Chen et al., 2023b; Qu et al., 2022). The ball transport in a wellbore can be regarded as coarse grain migration. The resolved CFD-DEM is particularly suitable for the situation compared to the unresolved method (Chen et al., 2024; Qu et al., 2023). It has scrutinized in a series of papers on fluidized beds and hydraulic conveying (Washino et al., 2023; Yamashiro and Tomac, 2022). Schnorr Filho et al. (2022) simulated the hydraulic transportation of coarse particles through a 90° elbow. Spheres measuring 6 mm in diameter and with a density of 1140 kg/m^3 were randomly generated at the inlet. The ratio of the pipe to ball diameter is 4.2. The results shed light on tactics for mitigating settling and grain accumulation in elbows, thereby improving the hydraulic conveyance of solid particles in industrial environments. Xiong et al. (2021) conducted a numerical study of the dynamic bridging process and the mechanism of particles becoming lodged in rectangular bend channels using the CFD-DEM approach. They examined the influence of particle concentration, particle density, channel geometry, and fluid dynamic viscosity on the bridging phenomenon. Particles with a diameter of 2 mm are easily bridged at the turn of the channel, especially at a large bend angle. Particle concentration is the critical factor that affects the probability of jamming. Wang and Liu (2020) investigated complex particulate flows with thermal convection in a fluidized bed to validate the effectiveness of the proposed the resolved CFD-DEM approach in modeling particulate flows involving both momentum exchange and thermal convection. The approach can accurately obtain the transport behavior of particles with different sizes. The CFD-DEM approach is highly suitable for modeling ball-sealer transport in vertical wellbores, especially under field pumping conditions. However, no studies or publications have specifically focused on this area to date.

Although ball sealers are widely utilized in hydraulic fracturing, the understanding of their transport behavior in vertical wells remains incomplete. This gap in knowledge is partly due to the numerous influencing factors and partly because the experimental parameters are significantly lower than those encountered in field conditions. This paper explores the intricacies of ball sealer transport and diversion in vertically perforated wells. The ball diversion experiment validates the CFD-DEM model and parameters. The effects of the ball position, injection flow rate, ball density, and flow rate ratio on plugging performance are studied. The transport of multiple balls and their plugging in between perforation clusters are discussed under field conditions. The objective is to clarify the transport behaviors and plugging performance of the ball sealer in vertical wells and identify best practices for its implementation.

2. Experimental and numerical method

2.1. Experimental device

Fig. 1 displays a schematic graph of the device to test the ball-sealer transport in an inclined pipe with six holes. A transparent acrylic pipe with an inner diameter of 50 mm and a length of 2 m is used to mimic the wellbore. The injection port side can be elevated, allowing for a wellbore with an inclination angle from 70° to 90°. The 90° indicates a horizontal wellbore. Six perforations with an inner diameter of 14 mm are used to simulate a perforation cluster, arranged in a helical pattern with a 60° phasing angle and a 60 mm spacing between the holes. These parameters match the actual field perforation specifications (Miskimins, 2019). The liquid flows through the perforations into buckets. The bucket is open, and the pressure at the hole outlet is equal to atmospheric pressure. After the test, the average flow rate for each hole can be determined. A high-speed camera is perpendicular to the hole section, recording ball transport.

2.2. Liquid and ball

Low-viscosity slickwater with a viscosity of 3 mPa s was prepared to be consistent with the fracturing fluid on site. In Fig. 2, the ball sealer (an acid copolymer) has a diameter of 13 mm and a density of 1180 kg/m^3, identical to the filed application (Angeles et al., 2012; Nozaki et al., 2013). The injection flow rate is 0.772 m^3/min in the 50 mm pipe, with a mean fluid velocity of 6.56 m/s. If the velocity remains constant, the equivalent flow rate in a 110 mm casing would be 3.73 m^3/min.

2.3. CFD-DEM equations

For ball transport in a vertical pipe, incompressible Navier–Stokes equations govern the fluid flow, and the mass and momentum formulas are given in Eqs. (1) and (2) (Shen et al., 2022). The immersed boundary (IB) method calculates interaction forces between Lagrangian points and surrounding fluid elements (Schnorr Filho et al., 2022). For the fluid phase, the coupled mass and momentum equations are solved using the pressure-implicit with splitting operators (PISO) method. A second-order QUICK scheme is employed to discretize the convective terms, while divergence and gradient terms are computed using a semi-implicit finite difference method.

$$\rho_{\mathrm{fl}}\frac{\partial \boldsymbol{u}_{\mathrm{fl}}}{\partial t} + \rho_{\mathrm{fl}}\left(\boldsymbol{u}_{\mathrm{fl}}\cdot\nabla\right)\boldsymbol{u}_{\mathrm{fl}} = -\nabla p + \mu_{\mathrm{fl}}\nabla^2\boldsymbol{u}_{\mathrm{fl}} \tag{1}$$

$$\nabla\cdot\boldsymbol{u}_{\mathrm{fl}} = 0 \tag{2}$$

the boundary condition

$$\boldsymbol{u}_{\mathrm{fl}} = \boldsymbol{u}_{\Gamma} \tag{3}$$

the initial condition

$$\boldsymbol{u}_{\mathrm{fl}}(x, t=0) = \boldsymbol{u}_0(x) \tag{4}$$

the ball–fluid interface condition on the ball boundary

$$\boldsymbol{u}_{\mathrm{fl}} = \boldsymbol{v}_{\mathrm{b}} \tag{5}$$

$$\sigma\cdot\boldsymbol{n} = \boldsymbol{t}_{\Gamma_{\mathrm{s}}} \tag{6}$$

Solid motions include translation and rotation, governed by Newton's second law.

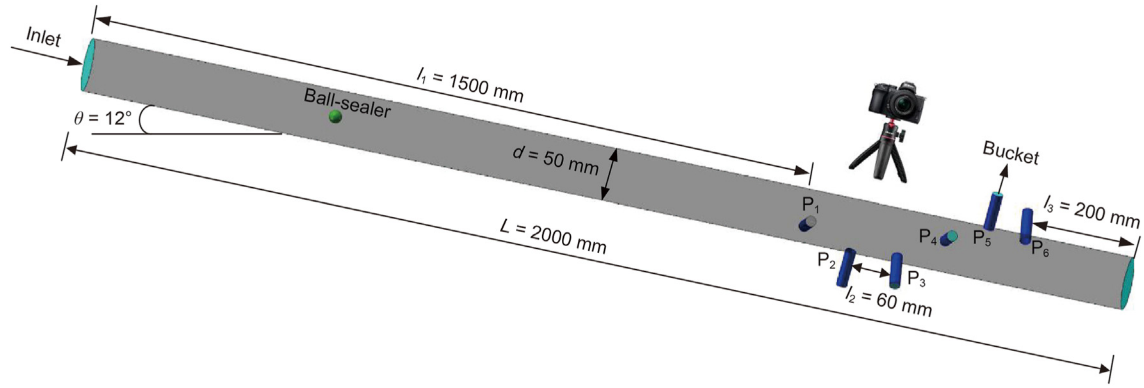

Fig. 1. Schematic of ball-sealer transport in an inclined pipe with six helical holes.

Fig. 2. Ball sealers.

$$m_b \frac{d\boldsymbol{v}_b}{dt} = m_b \boldsymbol{g} + \boldsymbol{F}_{b,f} + \sum \boldsymbol{F}_{b,w} \tag{7}$$

$$I \frac{d\omega_b}{dt} = \sum T_{c,w} + T_{b,f} \tag{8}$$

The force originating from the fluid on the ball sealer is expressed by Eq. (9)

$$\boldsymbol{F}_{b,f} = \sum_{c \in \overline{T}_h} \left(-\nabla p + \mu_{fl} \nabla^2 \boldsymbol{u}_{fl} \right) \cdot V \tag{9}$$

2.4. Numerical model

Fig. 3(a) shows the model of the vertical well with six holes. The vertical pipe has a diameter of 110 mm, simulating casing. Six side holes are arranged on the right side in a spiral distribution. The diameter of each hole is 12 mm, and the distance between adjacent holes is 60 mm, aligning precisely with the actual parameters specified for the experiment. The six holes serve as outlets, and the inlet is at the upper boundary of the pipe. The distance between the inlet and top perforation is 5 m to ensure sufficient fluid flow. Hexahedral elements are used to discretize the flow space. Dynamic meshing was used during the simulation process, and Fig. 3(b) illustrates an example of grid refinement employed in the simulation. The flow field influences the motion of the spheres in the fluid, and dynamic meshing adjusts the grid based on particle positions and velocities, ensuring accurate trajectory tracking. Dynamic meshing can adaptively adjust the mesh based on the characteristics of different scales, reducing computational costs while meeting the requirements of the analytical model (Washino et al., 2023).

2.5. Numerical method

In Table 1, the properties of the ball and fluid are set based on the field range. The time step is a crucial factor influencing the accuracy of the CFD-DEM model simulation. For DEM, the time step should be smaller than the distance travelled by the particle in a time step to ensure reasonable contact with the walls. The time step Δt_{DEM} is constrained by the time in Eq. (10).

$$\Delta t_{DEM} = \frac{\pi d_b / 2}{0.1631 \upsilon + 0.8766} \sqrt{\frac{2\rho_b (1+\upsilon)}{E}} \tag{10}$$

In CFD computations, the Courant number is a critical parameter to ensure numerical stability, as shown in Eq. (11). Typically, the Courant number should be kept below 1 for stability (Shen et al., 2022).

$$C_o = \frac{\boldsymbol{v}_f \Delta t_{CFD}}{\Delta x} < 1 \tag{11}$$

Due to the minimum length of fluid elements being 0.3 mm and the maximum fluid velocity being 15 m/s, C_o equals 0.5. Typically, the fluid phase's time step is ten times that of the solid phase. Δt_{DEM} is set to be 1×10^{-6} s, and Δt_{CFD} is set to be 1×10^{-5} s.

2.6. Simulation scheme

Table 2 lists the simulation scenarios where the parameter ranges are based on field conditions. The ball position indicates the distance between the ball and the perforation when the ball is located below the perforation. When the l_{bp} is 10 mm, the ball is closer to the hole. The total flow rate in the pipe will be split into the flow rate continuing through the wellbore and the flow rate diverting into the perforation. The flow rate ratio is the fluid flow rate through the perforation to that upstream of the perforation, expressed by Eq. (12).

$$R_p = \frac{Q_{pi}}{Q_p} \times 100\% \tag{12}$$

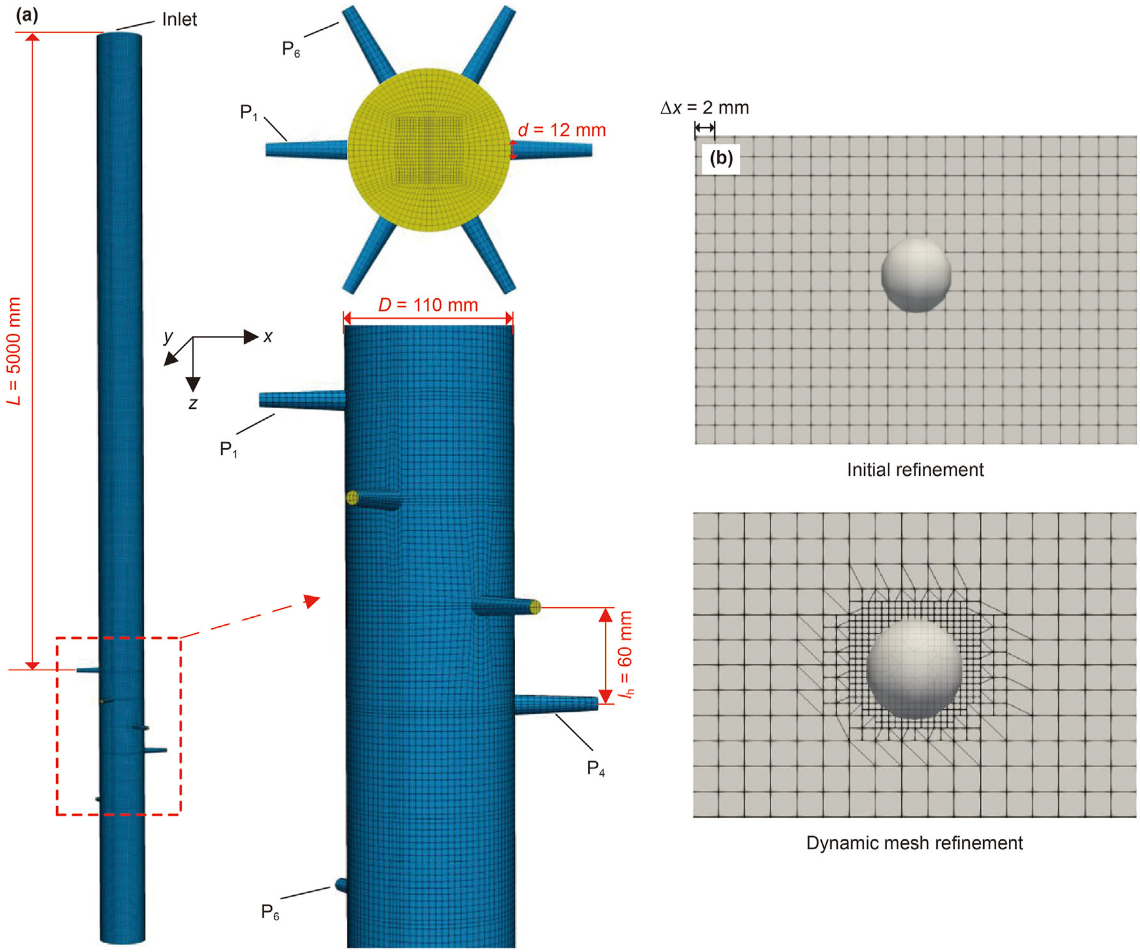

Fig. 3. Model sizes and fluid cells.

Table 1
Parameters for numerical model.

Type	Parameter	Numerical value	Field value
Fluid properties	Inlet velocity $\mathbf{v}_f$, m/s	4–15	2–20
	Density ρ_f, kg/m^3	1000	
	Dynamic viscosity μ_f, Pa s	0.003	0.001–0.005
Ball-sealer properties	Diameter d_b, mm	13	6–16
	Density ρ_b, kg/m^3	1100–1300	
	Young's modulus E, Pa	9×10^7	10^6–10^9
	Poisson's ratio v_p	0.32	0.25–0.50
	Restitution coefficient e	0.5	/
	Sliding friction coefficient μ_s	0.5	/
	Rolling friction coefficient μ_r	0.05	/

Table 2
Simulation scheme.

Case	Ball position l_{bp}, mm	Flow ratio R_p, %	Fluid velocity v_f, m/s	Flow rate Q_p, m^3/min	Ball sealer density ρ_b, kg/m^3	Inclination angle θ_w, °
1	20–55	0.167	4.0	2	900–1300	0
2	30	0.1–0.5	4.0	2	900–1300	0
3	30	0.167	4.0–14.8	2–7	900–1300	0

where Q_{pi} is the flow rate of the perforation i, m^3/min; Q_p is the injection flow in the wellbore, m^3/min.

3. Validation of the numerical model

The numerical model and mesh size significantly affect ball transport behavior and should be validated by experimental results.

The model's dimensions are identical to the experimental device, and fluid and ball properties are consistent with the experiment. The mesh in the perforation section is refined and optimized to ensure the mesh independence. Three wellbore models are established with the cube length from 2 to 6 mm. It is found that ball motion is highly sensitive to the grid size. In Fig. 4, mesh independence is validated by comparing the ball trajectories around the P_2. The high-velocity ball with large inertia misses the P_1 and transports toward the P_2 due to the influence of flow diversion. When the mesh length is over 2 mm, the ball misses the P_2 and hits the downstream wall, indicating inaccurate fluid flow around the P_2 entrance. The drag force toward the P_2 is not enough, and the ball cannot turn in time. Thus, the 2 mm length of the cubic element is rational. Before the first perforation of P_1, the ball position is stable, and the length of 1.35 m between the inlet and the P_1 is enough for the fully developed flow regime.

The inclination angle is 78°, and the orientation of the P_2 is downward. The injection flow rate is 0.772 m^3/min at the inlet, and the fluid rates in the six holes are almost identical. Fig. 5 shows the process of the ball diversion to the P_4. The ball sealer is suspended in the middle of the pipe and transported to the hole section without settling to the bottom. The ball quickly passed through the P_1—P_3 section and reached the right side of the P_4. At t_1, the ball was no longer moving towards the wellbore bottom. Then, it turned to the P_4 due to the fluid diversion. At t_3, it flowed into the P_4 and was stopped by a step inside the hole. The ball trajectories around the P_4 are identical to the experimental results at three moments. The ball missed the P_4 a little distance due to inertia, then turned and blocked the P_4. Vector arrows indicate the fluid flow, and the simulation fluid velocity of the hole exit is 14.0 m/s, similar to the experimental velocity of 13.9 m/s.

Fig. 6 shows the process of the ball entering the downward hole of the P_2. In the experiment, as the ball sealer was suspended and transported in the lower part of the pipeline, it was prone to enter the heel-side downward hole of P_2. The reason is that the drag force is generated by fluid diversion and the ball's gravity is downward. The numerical results accurately display the experimental process.

4. Result and analysis

4.1. Ball position l_{bp}

Once the ball sealer enters the wellbore, it travels downwards

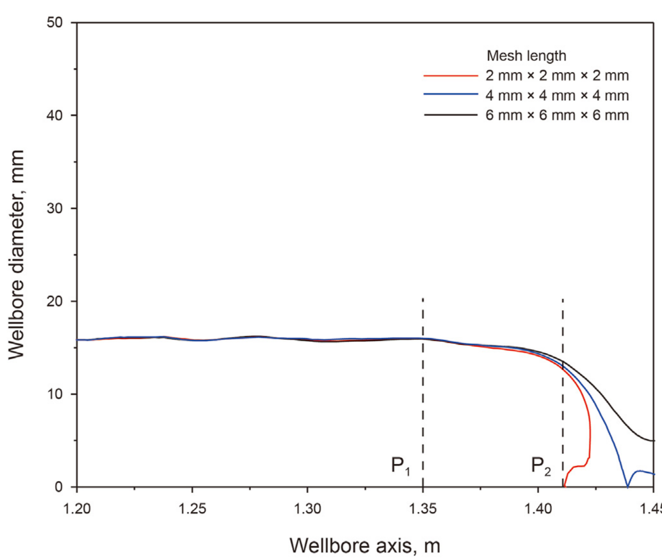

Fig. 4. Mesh independence validation.

for thousands of meters. Due to the influence of liquid flow and wellbore trajectory, the horizontal position of the ball in the wellbore is variable. The relative position between the ball and perforation significantly impacts the plugging performance (Yuan et al., 2022). Fig. 7 illustrates three scenarios where the distance (l_{bp}) between the ball sealer and the P_1 is reduced from 55 to 30 mm. The liquid enters the inlet at a velocity of 4.2 m/s, gradually decelerating as it exits through six perforations. There is a clockwise vortex at the lower boundary due to fluid compression. In Fig. 7(a), as the ball sealer enters the perforation section, it experiences disruption from the liquid diverting into the perforation, causing its trajectory to the horizontal shift. Upon entering the lower-speed area of the wellbore, it loops back to plug the P_6. In Fig. 7(b), with a distance of 32 mm between the ball sealer and the P_1, the small ball's trajectory is significantly influenced by the fluid flow around the P_1. However, after colliding with the pipe wall, the small ball misses the P_1 and flows downwards. In Fig. 7(c), the ball successfully diverts to the P_1 and plugs it. A ball is prone to plug when close enough to the perforation.

Fig. 8(a1) and (b1) show enlarged views around the P_1, marked by red dashed boxes in Fig. 7(b) and (c). Due to fluid diversion, a region of velocity variation forms around the entrance of P_1, where the fluid velocity rapidly increases. As the ball-sealer approaches the P_1, fluid diversion to the P_1 generates a drag force, dragging the ball towards the P_1. When the l_{bp} is 32 mm, the ball is located at the edge of the region, but the drag force is insufficient to cause the ball to turn quickly to the P_1. When the l_{bp} is 30 mm, the ball resides within the region, and the drag force causes it to plug into the P_1. Hence, 30 mm is a threshold distance.

Fig. 8(a2) and (b2) illustrate two velocities of the ball migration, including the velocity along the wellbore axis ($\boldsymbol{V}_z$) and the velocity towards the P_1 ($\boldsymbol{V}_p$). Noted that the P_1 is located at 5.0 m in the z-axis direction of the wellbore. At 4.95 m in the z-axis direction, the $\boldsymbol{V}_p$ begins to increase. For $l_{bp} = 30$ mm, $\boldsymbol{V}_p$ significantly increases from 0 to 2.41 m/s, while $\boldsymbol{V}_z$ remains relatively stable. However, when the l_{bp} is 33 mm, $\boldsymbol{V}_p$ increases from 0 to 1.77 m/s. This outcome underscores that the position of the ball sealer is crucial for successful plugging. The ratio of $\boldsymbol{V}_p$ to $\boldsymbol{V}_z$ indicates the trajectory's deviation from its initial path, as shown in Eq. (13). The diversion index (S_R) is the integral of R to evaluate the plugging performance of the ball-sealer, as shown in Eq. (14). When l_{bp} decreases from 32 to 30 mm, the S_R increases from 0.0077 to 0.0099. The larger the S_R, the faster the ball turns and plugs the perforation.

$$R = \frac{\boldsymbol{V}_p}{\boldsymbol{V}_z} \tag{13}$$

$$S_R = \int_0^5 R dx \tag{14}$$

Fig. 9 shows the correlations between S_R and l_{bp} at the three densities, including buoyant and nonbuoyant balls. Solid symbols indicate a successful plugging. The ball will plug the hole once the l_{bp} is less than the threshold distance. The buoyant with a density of 900 kg/m^3 ball has a similar plugging performance to the nonbuoyant ball with a density of 1100 kg/m^3, and the threshold of l_{bp} is 30 mm, as shown in Fig. 9(a). For the ball with a density of 1300 kg/m^3, the threshold value is 28 mm. Fig. 9(b) shows the transport trajectories of three balls. As the l_{bp} is 30 mm, the ball with a density of 1300 kg/m^3 misses the hole, while the low-density balls can plug the hole.

In a vertical well, the closer the ball sealer is to the wellbore wall, the greater the likelihood of successfully plugging the perforation. The ball weight is small. Also, the transport direction is same as the

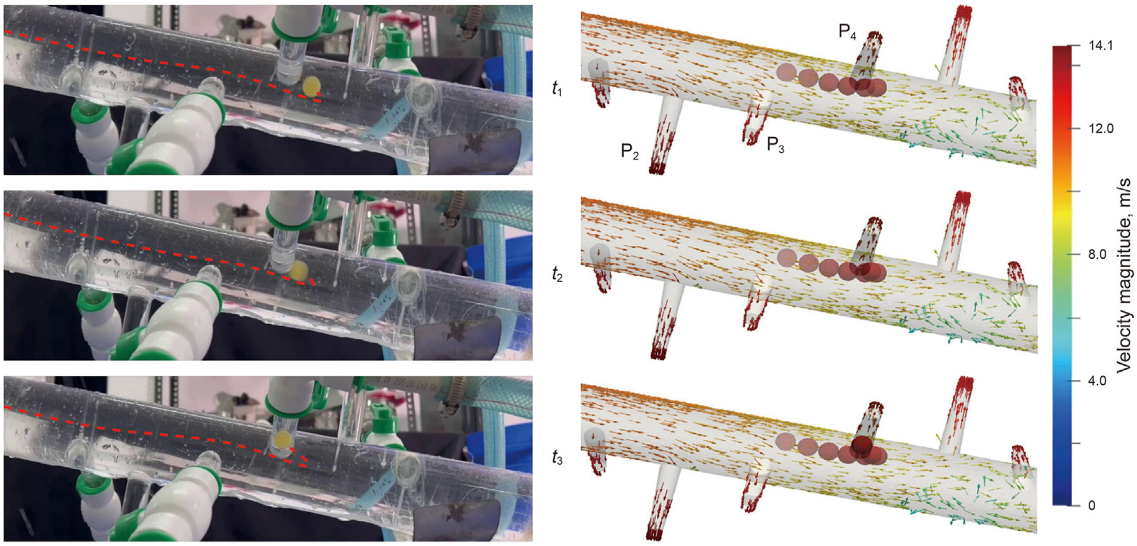

Fig. 5. Ball-sealer transport in the inclined pipe and plugging on the P_4.

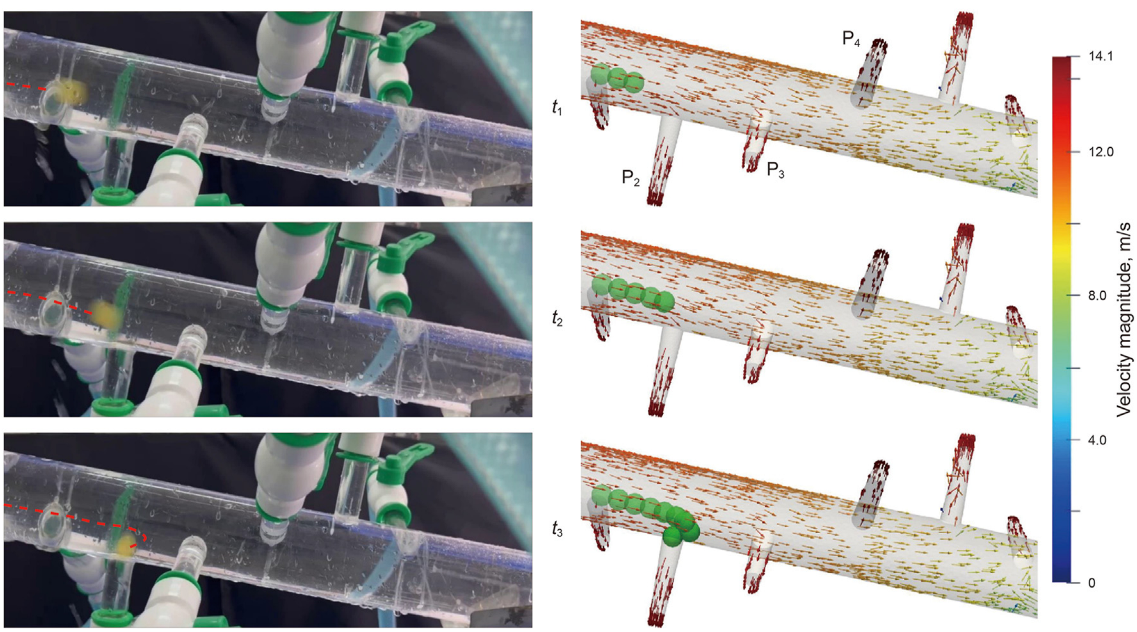

Fig. 6. Ball sealer transport in the inclined pipe and plugging on the P_2.

gravity in the vertical well. Thus, the density has minimal influences on the diversion plugging, and the lighter ball with a smaller inertia force toward the wellbore axis has a better plugging performance. Low-density balls can enhance plugging performance to some extent.

4.2. Flow rate ratio R_p

Measurements from disposable fiber optics and downhole video cameras provide sufficient evidence of a significant flow rate difference between the perforations. Preferential perforations receive more fracturing liquid, while some do not have liquid (Savitski et al., 2024). In Fig. 10, the injection flow rate is 2 m^3/min, and the flow rate of P_1 varies from 0.334 to 1 m^3/min. In Fig. 10(a1), the ball misses the perforation and collides with the wall behind the hole. In Fig. 10(b1), the flow rate of the P_1 decreases, and a region of velocity variation around the P_1 decreases. The ball is not located in the region, making it difficult to turn to the P_1. When the R_p increases to 0.5, the high-speed fluid exerts a significant drag force on the ball, overcoming the inertia force in the vertical direction, and the ball plugs the perforation, as shown in Fig. 10(a2). The ball rapidly diverts towards the perforation with the high-flow rate. In Fig. 10(b), as the flow rate ratio increases, the area of velocity variation around the hole becomes more considerable. Therefore, the ball is more likely to plug the perforation with a larger flow rate ratio.

Fig. 11(a) illustrates the ball's velocity variation towards the perforation as the flow rate increases from 0.1 to 0.5. When R_p is 0.5, $\boldsymbol{V}_p$ increases from 0 m/s at $z = 4.2$ m to 17 m/s at $z = 5.0$ m, and the ball plugs the perforation rapidly. However, when R_p is 0.1, $\boldsymbol{V}_p$ increases at $z = 4.7$ m and achieves the maximum value of 1.06 m/s at the P_1. It indicates that the drag force in the $\boldsymbol{V}_p$ direction cannot overcome the inertia force, resulting in a slower turning speed. In Fig. 11(b), the diversion performance gradually improves with the

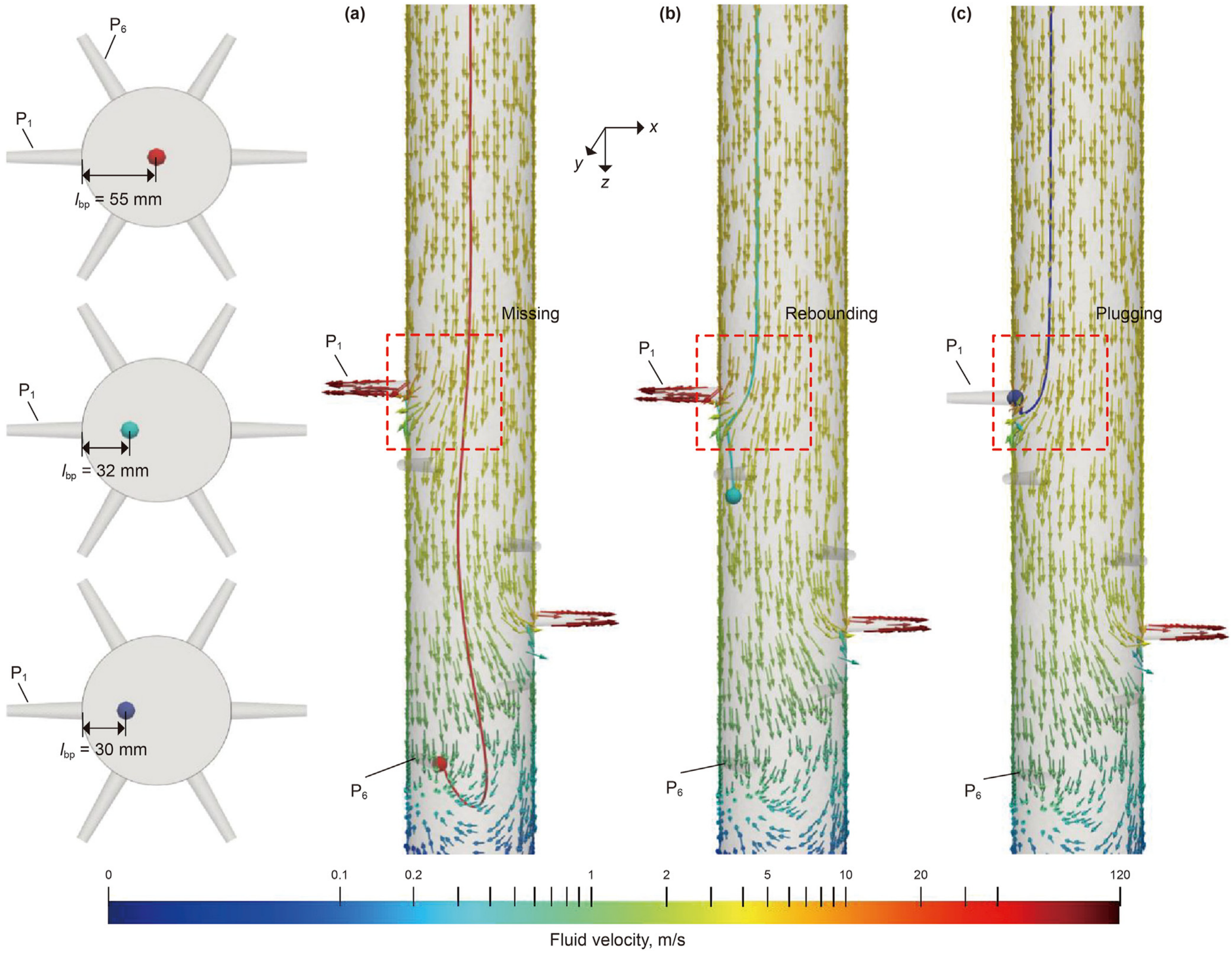

Fig. 7. Ball sealer transport in the vertical well at three positions of Case 1 (Table 1), front view.

increase in the R_p. The threshold of the R_p exceeds 0.167, with a corresponding diversion index of 0.01. When the R_p exceeds 0.167, the ball will rapidly divert and plug the hole. Due to smaller inertia, the buoyant ball is slightly easier to plug than the nonbuoyant.

As the ball's position is crucial, the relationship between R_p and l_{bp} is calculated to determine the blocking area. The critical flow rate ratio for different positions is obtained based on many simulations. In Fig. 12, the area to the left of the R_p critical curve is the blocking area. Fig. 12(b) shows the ball trajectories of two particular scenarios in Fig. 12(a). As the R_p is 0.1, the l_{bp} should be no more than 15 mm. When the l_{bp} is 78 mm, the R_p should increase to 0.95, and the ball plugs the hole, even if it moves to the lower region.

The ball sealer will likely plug the perforation in a wellbore with a large flow rate. However, the fracturing layer has many perforations, and the average Q_p of each perforation might be very small. The balls easily miss the hole, and the perforation scheme significantly decreases the plugging performance. The result will guide the completion design, including optimizing perforation parameters and designing the ball sealer process.

4.3. Injection flow rate Q_p

During the ball delivery stage, the injection flow rate significantly affects the ball transport behavior and plugging performance (Tan et al., 2018). With a high flow rate, the ball moves quickly, making it difficult to navigate and seal the perforation, resulting in a slight increase in surface pressure. With a low flow rate, the ball does not move with the fluid and might not plug the perforation. In Fig. 13, the ball plugs the perforation when the flow rate is 2 m^3/min. When the flow rate increases to 7 m^3/min, the average fluid velocity is 14.8 m/s, and the ball has a large inertia. As the ball approaches the perforation, its trajectory is altered by the diversion effect toward the perforation direction. However, it fails to plug the perforation and instead collides with the surface behind the perforation. Fig. 14 compares the diversion indexes at two flow rates. When the ball sealer moves to 4.4 m, the $\boldsymbol{V}_p$ starts to increase until it plugs the hole, the $\boldsymbol{V}_p$ increases from 0 m/s at 4.2 m to 2.41 m/s at 5 m, and S_R is 0.0099. In Fig. 14(b), $\boldsymbol{V}_p$ increases from 0 m/s at 4.5 m to 5.1 m/s at 5 m, while $\boldsymbol{V}_z$ remains almost unchanged at 15.58 m/s. Since the $\boldsymbol{V}_z$ is large, the diversion index decreases to 0.0067, and the ball needs more time to turn to the perforation. At high injection flow rates, the ball's inertia is significant, making it difficult to quickly change direction and plug the perforation, causing it to continue moving along its original path.

In Fig. 15(a), the threshold of the Q_p for high-density balls is 4 m^3/min, while for low-density balls, it is 4.2 m^3/min. When the Q_p is less than 4 m^3/min, the liquid flowing towards the perforation greatly influences on the ball diversion, significantly improving the

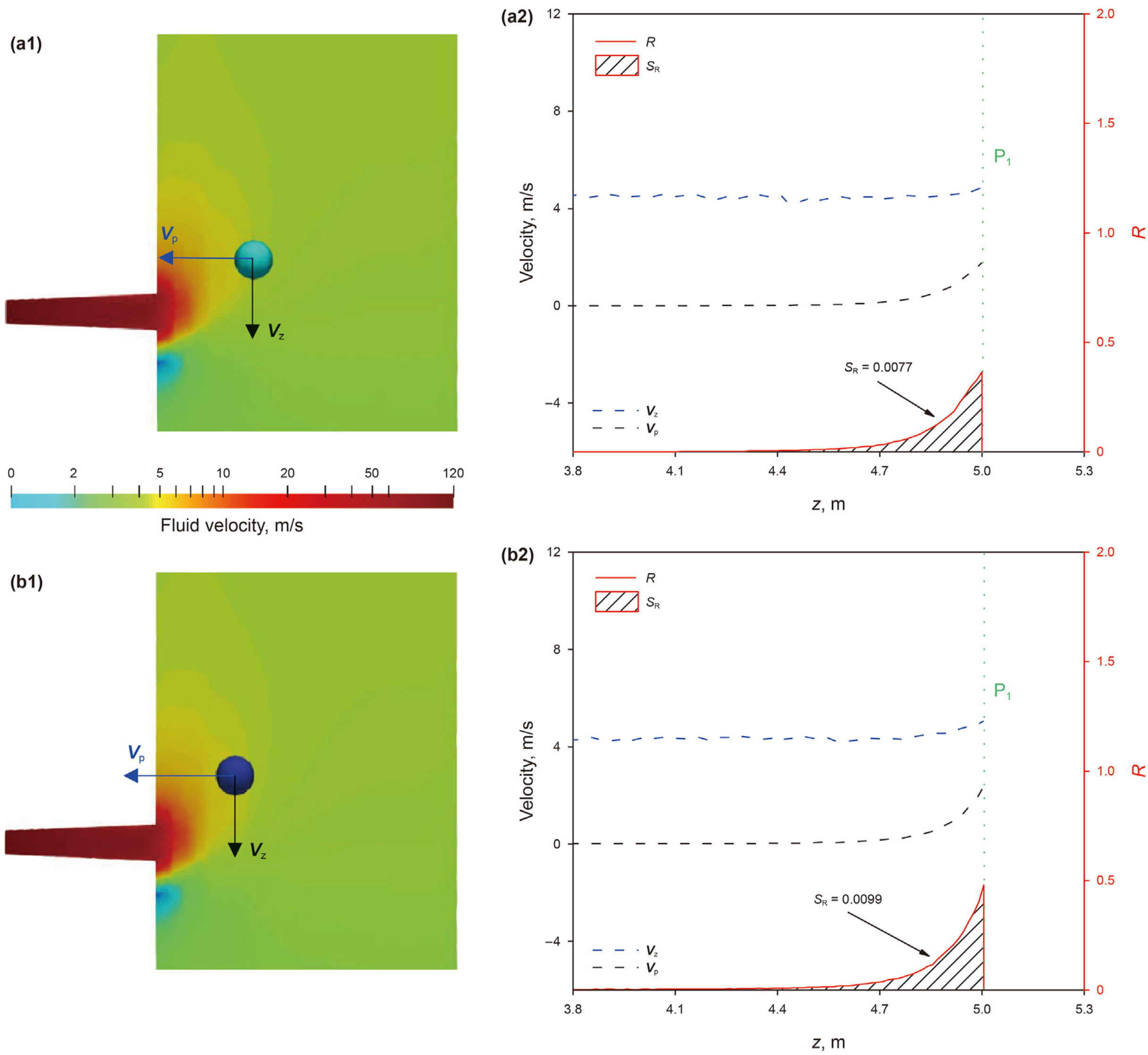

Fig. 8. Ball-sealer transport around the P_1 in Fig. 7, enlarged view. (**a**) $l_{bp} = 32$ mm; (**b**) $l_{bp} = 30$ mm.

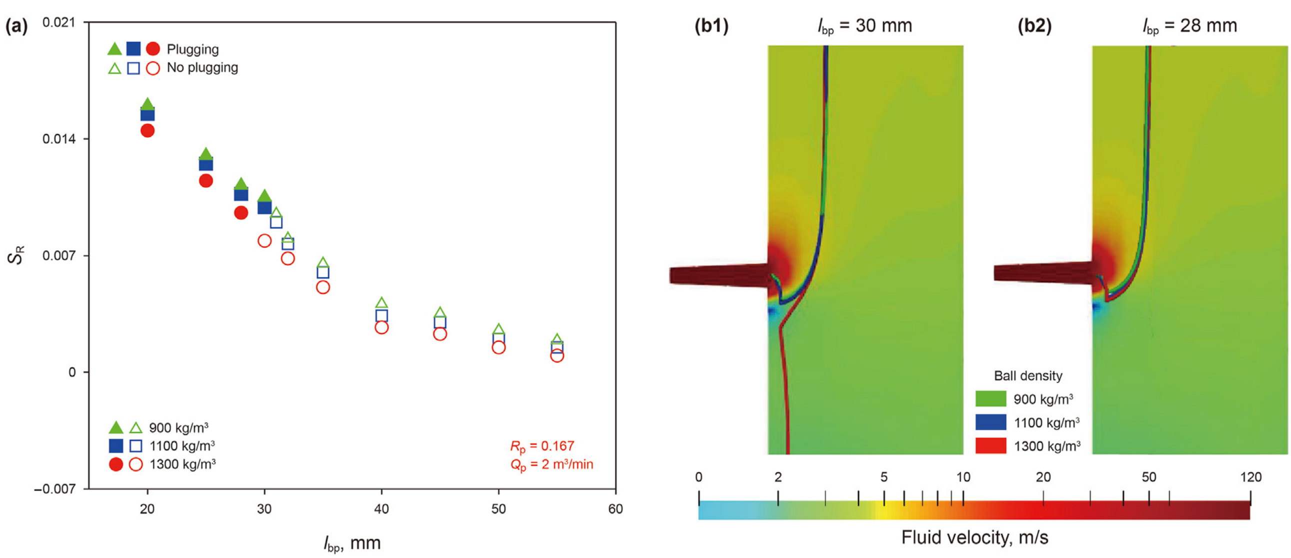

Fig. 9. (**a**) Correlations between S_R and l_{bp} at the three densities of ball sealers; (**b**) Fluid velocity contour and ball trajectories, enlarged view of P_1.

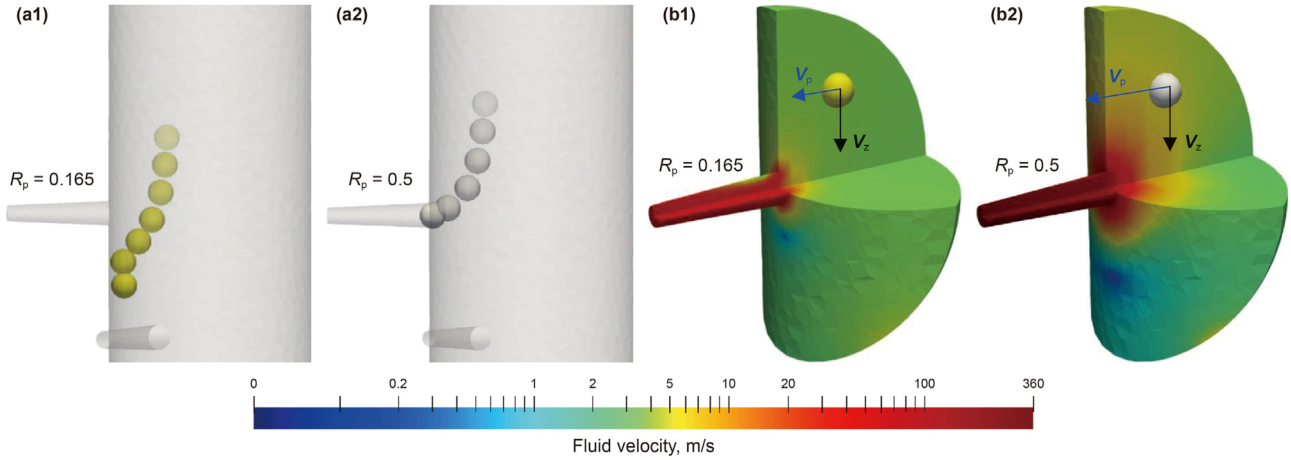

Fig. 10. Ball transport around the perforation at $Q_p = 2$ m^3/min, $l_{bp} = 30$ mm, $\rho_b = 1100$ kg/m^3. (**a**) Ball trajectory around the perforation; (**b**) Snapshots of ball transport.

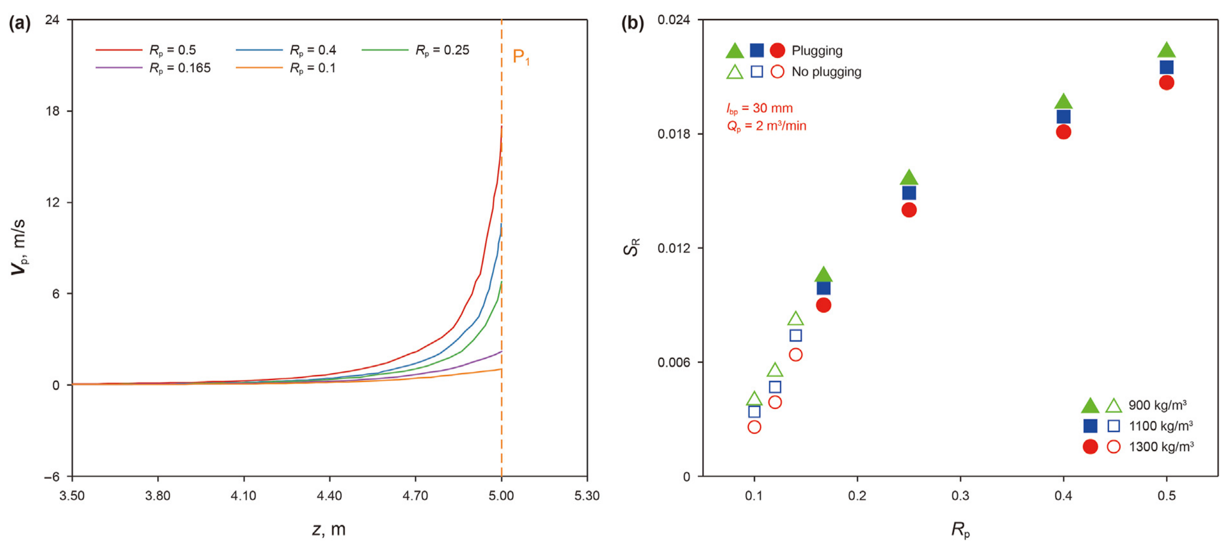

Fig. 11. (**a**) Variations of V_p at different flow rates; (**b**) Correlations between S_R and R_p at the three densities of ball sealers.

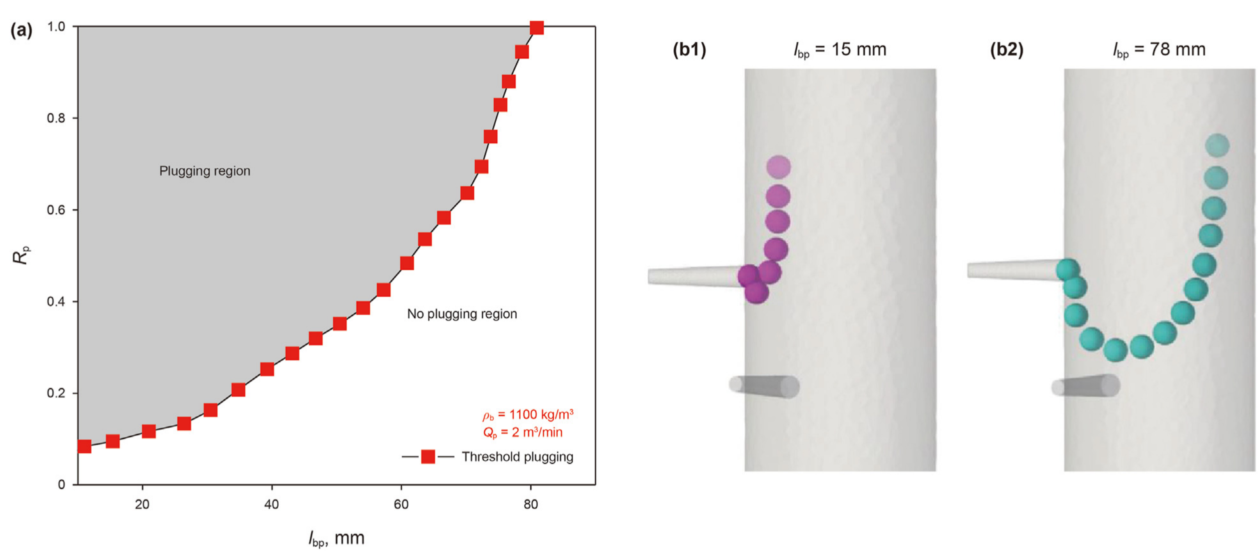

Fig. 12. (**a**) Plugging area at different threshold lengths at the density of 1100 kg/m^3; (**b**) Ball trajectories for plugging.

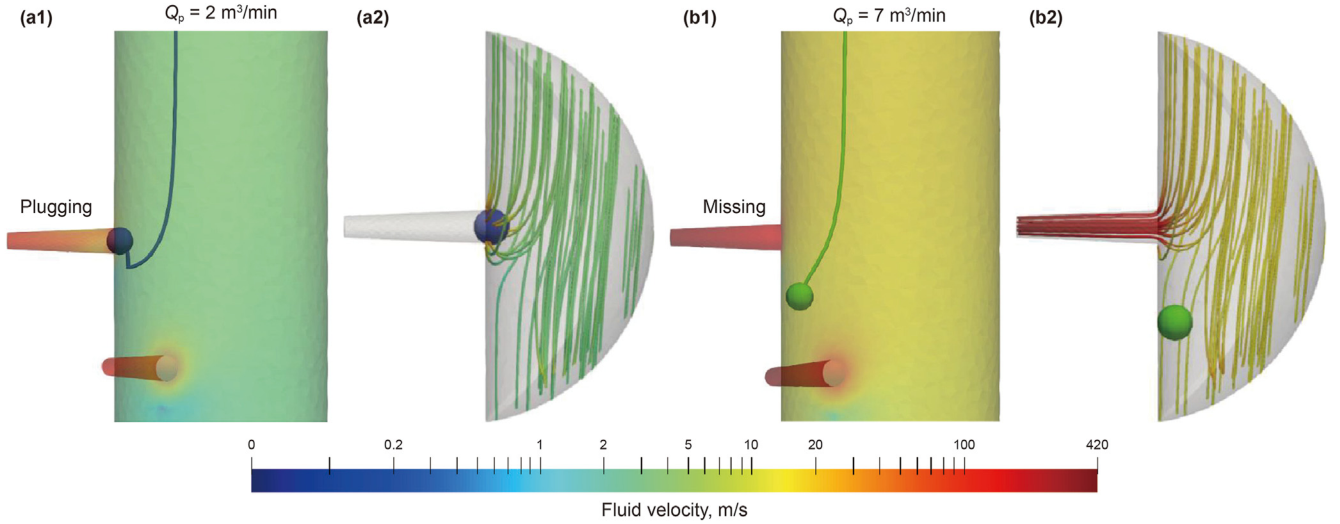

Fig. 13. Ball transport around the perforation at $l_{bp} = 30$ mm, $\rho_b = 1100$ kg/m^3. (**a**) $Q_p = 2$ m^3/min; (**b**) $Q_p = 7$ m^3/min.

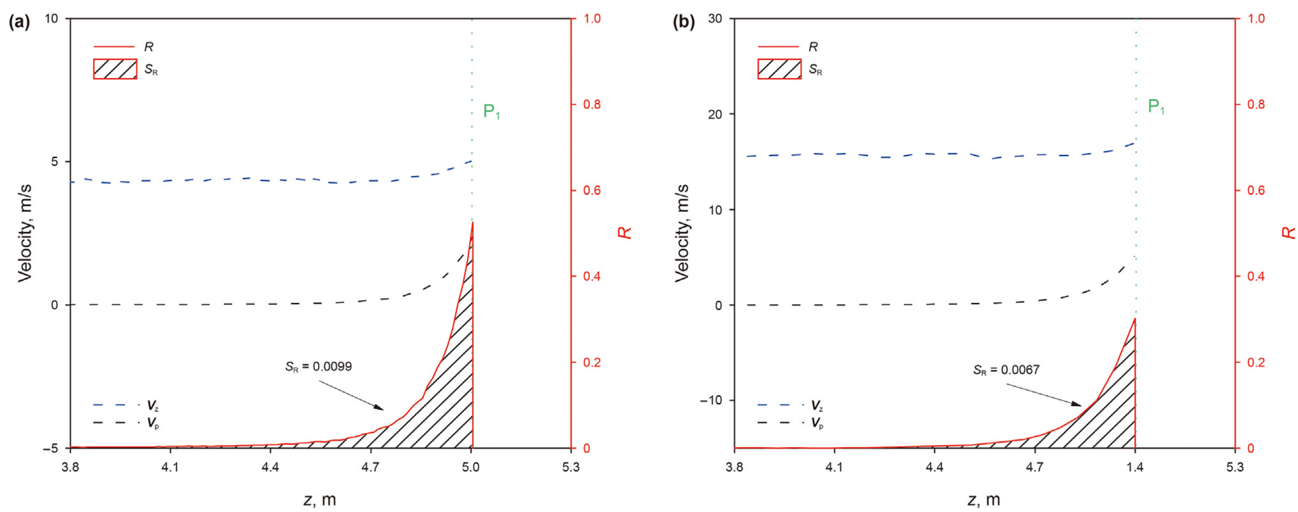

Fig. 14. The velocities of the ball sealer in two directions. (**a**) $Q_p = 2$ m^3/min; (**b**) $Q_p = 7$ m^3/min.

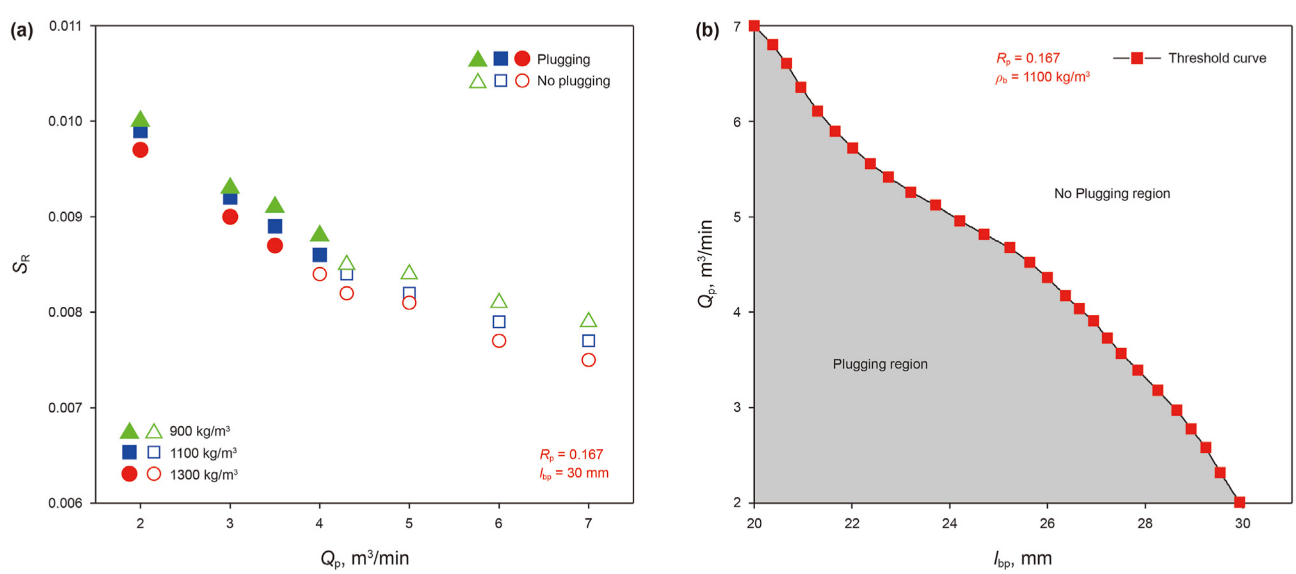

Fig. 15. (**a**) Correlations between S_R and Q_p at the three densities of ball sealers; (**b**) Plugging area at different threshold lengths.

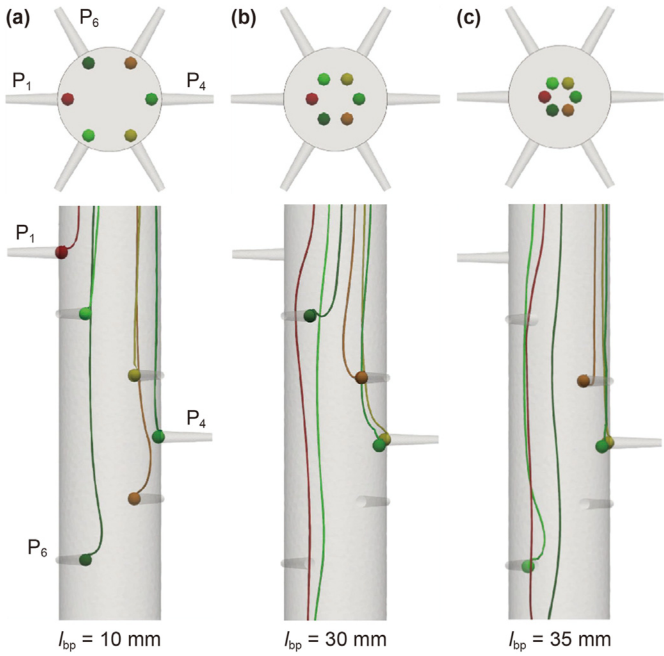

Fig. 16. Ball plugging in a six-perforation cluster at $Q_p = 2$ m^3/min, $\rho_b = 1100$ kg/m^3, $R_p = 16.6\%$.

plugging performance. Fig. 15(b) shows the plugging region by calculating the relationship between Q_p and l_{bp}. When the Q_p exceeds 6 m^3/min, the l_{bp} should be less than 22 mm to achieve successful plugging.

The results indicate that, in many cases, increasing the injection rate alone will not improve the plugging performance. The method will increase the drag force toward the hole, and it also increases the ball inertia. A low injection rate may increase the plugging performance. Thus, the engineer continuously optimizes the ball delivery rate based on the pressure response after plugging perforations, obtaining a flow rate range for the target block.

5. Discussion

5.1. Interaction between balls

The mutual interactions between balls can change their relative position during the downward transport. Fig. 16 shows ball transport in a vertical well at three initial positions. In Fig. 16(a), six balls are placed 10 mm from the wellbore wall at the inlet. After a 5-m migration, the ball plugs the corresponding perforation. In Fig. 16(b), the ball misses the P_1, P_5, and P_6 due to the increased distance. Since the threshold of l_{bp} is 30 mm for a single ball, the phenomenon of mutual interaction is proven. Also, the red ball aligned with the P_5 plugs the P_4. Its trajectory is affected by other ball migration and perforation attraction. In Fig. 16(c), three perforations are plugged as the l_{bp} is 35 mm. Mutual repulsion occurs because of the small distance between adjacent balls, changing the orientation and distance between the hole and ball. In Fig. 17(a), the minimum percentage is 50% at a ratio of 1:1, identical to the literature (Nozaki et al., 2013). The top P_1 is hardly plugged, possibly due to the large inertia.

5.2. Interaction between clusters

Fig. 17(b) shows the plugging percentage at the upper cluster in a vertical well with two perforation clusters. The smaller the flow rate ratio of the top cluster, the lower the plugging percentage, and the balls transport to the lower cluster. When the cluster receives 20% of the injection liquid, the plugging percentage is 16.7%, and only one hole is plugged. Typically, the minimum horizontal stress gradually increases with the burial depth, and a hydraulic fracture is easily generated at the shallow cluster. Based on the research, increasing the number and diameter of perforations in the shallow cluster is recommended to ensure a large flow rate ratio and a good fracturing effect. Then, ball sealers are prone to plug more perforations in the upper cluster, diverting fluid to the lower cluster. This approach helps prevent excess balls from bypassing the upper cluster and blocking under-stimulated lower perforations. It induces high fracturing pressures and insufficient fluid entry, affecting fracture propagation.

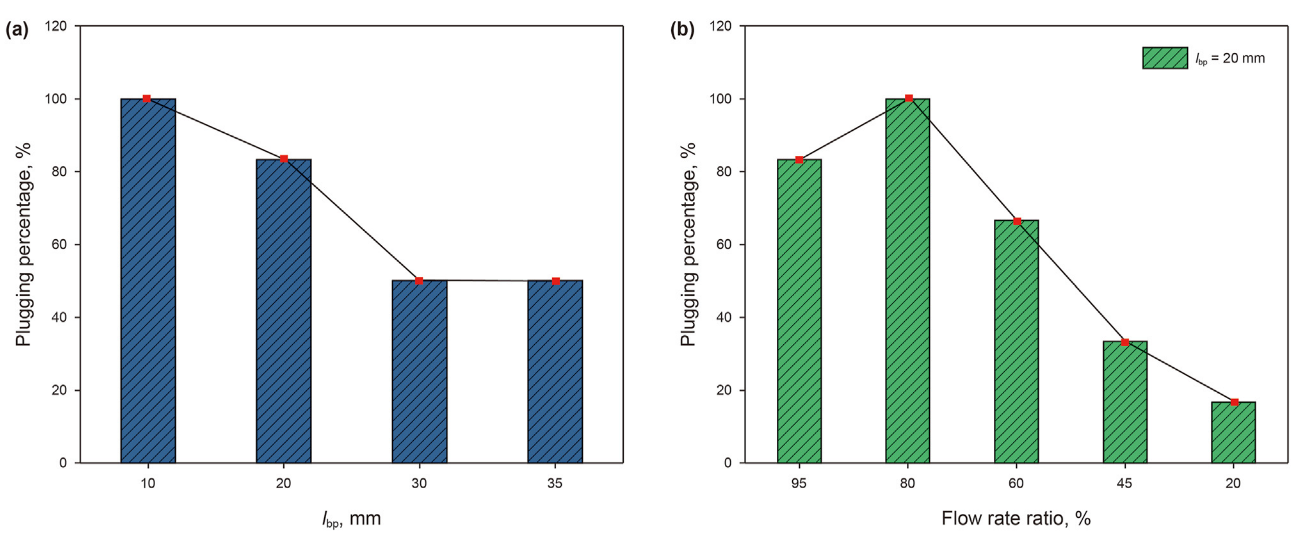

Fig. 17. (**a**) Relationship between the plugging percentage and l_{bp}; (**b**) Relationship between the plugging percentage and flow rate ratio between two perforation clusters.

6. Conclusions

This study investigates the dynamics of ball sealer plugging performance in perforations under a range of field conditions, providing valuable insights into ball plugging. The main findings can be summarized as follows:

(1) Plugging performance improves with an increased flow rate ratio, whether for a single perforation or a cluster. Even when the ball sealer is initially distant from the perforation, a sufficiently high flow rate ratio can cause it to divert by 90° and effectively plug the perforation.
(2) There exists a threshold distance between the ball and the perforation under specific conditions. The closer the ball sealer is to the wellbore wall, the higher the likelihood of successful plugging. The plugging performance of balls with a density of 900 kg/m^3 is better than that of balls with a density of 1300 kg/m^3.
(3) At high injection flow rates, the ball's inertia becomes significant, making it difficult to quickly change direction and plug the perforation, causing it to continue on its original path. Lower flow rates can improve plugging performance, and a recommended flow rate range is 2–4 m^3/min.
(4) Interactions between multiple balls can affect their positions, which in turn alters the relative distance between the balls and the perforations, leading to variations in the plugging performance of the perforations.
(5) In vertical wells with multiple perforation clusters, it is crucial to ensure that the first fracturing cluster receives a higher flow rate to improve plugging performance. This prevents excessive balls that miss the first cluster from plugging under-stimulated perforations in lower clusters.

CRediT authorship contribution statement

Ying Liu: Writing – original draft, Investigation, Data curation. **Hai Qu:** Supervision, Methodology, Funding acquisition. **Mao Sheng:** Visualization, Software, Methodology. **Hai-Zhu Wang:** Visualization, Resources, Methodology. **Ting-Xue Jiang:** Methodology, Investigation, Conceptualization. **Shi Wang:** Investigation, Formal analysis.

Declaration of competing interest

The authors declare that they have no known competing financial interests or personal relationships that could have appeared to influence the work reported in this paper.

Acknowledgments

This work is supported by the National Natural Science Foundation of China (Grant No. 52274035).

Nomenclature

$\boldsymbol{u}_{\mathrm{fl}}$	Fluid velocity, m/s
μ_{fl}	Fluid viscosity, Pa s
ρ_{fl}	Fluid density, kg/m^3
$\boldsymbol{v}_{\mathrm{b}}$	Particle velocity, m/s
$\boldsymbol{u}_{\Gamma}$	Boundary condition for the fluid velocity, m/s
$\boldsymbol{u}_0$	Initial condition for the fluid velocity, m/s
σ	Stress tensor
$\boldsymbol{n}$	Unit vector normal to the solid surface
$\boldsymbol{t}_{\Gamma\mathrm{s}}$	Traction vector of the fluid
$\boldsymbol{g}$	Gravity, m/s^2
m_{b}	Mass of particle, kg
ω_{b}	Particle angular velocity, rad/s
I	Moment of inertia of the particle, kg m^2
$T_{\mathrm{c,w}}$	Contact torque of particle to wall, N m
$T_{\mathrm{b,f}}$	Torque caused by fluid, N m
$\boldsymbol{F}_{\mathrm{b,f}}$	Force contribution caused by the fluid on particle
$\boldsymbol{F}_{\mathrm{b,w}}$	Ccontact force of particle to wall
V	Volume of the fluid cell, m^3
Δl	Transport distance between two frames, m
Δt	Time interval between two frames, s

References

Angeles, R., Tolman, R., Ross, K., Burnham, H., El-Rabaa, W., 2012. First application of just-in-time perforating in a horizontal well. In: SPE Hydraulic Fracturing Technology Conference. https://doi.org/10.2118/152100-MS.
Bilden, D.M., Lacy, L.L., Seiler, F.H., Ischy, N.D., Fox, C.S., 1998. New water-soluble perforation ball sealers provide enhanced diversion in well completions. In: SPE Annual Technical Conference and Exhibition. https://doi.org/10.2118/49099-MS.
Brown, R.W., Neill, G.H., Loper, R.G., 1963. Factors influencing optimum ball sealer performance. J. Petrol. Technol. 15 (4), 450–454. https://doi.org/10.2118/553-PA.
Chen, X., Li, Y., Liu, Z., et al., 2023a. Visualized investigation of the immiscible displacement: influencing factors, improved method, and EOR effect. Fuel 331, 125841. https://doi.org/10.1016/j.fuel.2022.125841.
Chen, X., Li, Y., Liu, Z., et al., 2023b. Experimental and theoretical investigation of the migration and plugging of the particle in porous media based on elastic properties. Fuel 332, 126224. https://doi.org/10.1016/j.fuel.2022.126224.
Chen, X., Li, X., Wu, P., et al., 2024. Pore-scale transport dynamic behavior of microspheres and their mechanisms for enhanced oil recovery. Energy Fuels 38 (4), 2803–2815. https://doi.org/10.1021/acs.energyfuels.3c03931.
Cheng, W., Lu, C., Feng, G., Xiao, B., 2021. Ball sealer tracking and seating of temporary plugging fracturing technology in the perforated casing of a horizontal well. Energy Explor. Exploit. 39 (6), 2045–2061. https://doi.org/10.1177/01445987211020414.
Erbstoesser, S.R., 1980. Improved ball sealer diversion. J. Petrol. Technol. 32 (11), 1903–1910. https://doi.org/10.2118/8401-PA.
Gabriel, G.A., Erbstoesser, S.R., 1984. The design of buoyant ball sealer treatments. In: SPE Annual Technical Conference and Exhibition. https://doi.org/10.2118/13085-MS.
Liu, S., Zhang, Y., Du, H., et al., 2023. Experimental study on fluid flow behaviors of waterflooding fractured-vuggy oil reservoir using two-dimensional visual model. Phys. Fluids 35 (6), 062106. https://doi.org/10.1063/5.0152685.
Miskimins, J., 2019. Hydraulic Fracturing: Fundamentals and Advancements. Society of Petroleum Engineers, Richardson, TX, USA. https://doi.org/10.2118/9781613997192.
Nozaki, M., Zhu, D., Hill, A.D.D., 2013. Experimental and field data analyses of ball-sealer diversion. SPE Prod. Oper. 28 (3), 286–295. https://doi.org/10.2118/147632-PA.
Qu, H., Liu, Y., Lin, H., et al., 2022. 3D CFD-DEM simulation and experiment on proppant particle-fluid flow in a vertical, nonplanar fracture with bends. Int. J. Multiphas. Flow 146, 103873. https://doi.org/10.1016/j.ijmultiphaseflow.2021.103873.
Qu, H., Chen, X., Hong, J., et al., 2023. Experimental and 3D numerical investigation on proppant distribution in a perforation cluster involving the artificial neural network prediction. SPE J. 28 (4), 1650–1675. https://doi.org/10.2118/214316-PA.
Qu, H., Liu, Y., Li, C., et al., 2024a. Experimental and simulation investigation on ball-sealer transport and diversion performance aided by machine learning method. SPE J. 29 (2), 725–741. https://doi.org/10.2118/218010-PA.
Qu, H., Zeng, Z., Liu, Y., et al., 2024b. Experimental and simulation investigations of proppant transport and distribution between perforation clusters in a horizontal well. SPE J. 29 (10), 5286–5304. https://doi.org/10.2118/223087-PA.
Savitski, A.A., Lock, B., Todea, F., et al., 2024. Improving stage isolation in vaca muerta wells through observations from an integrated fiber optic pilot. In: SPE Hydraulic Fracturing Technology Conference and Exhibition. https://doi.org/10.2118/217785-MS.
Schnorr Filho, E.A., Lima, N.C., Franklin, E.M., 2022. Resolved CFD-DEM simulations of the hydraulic conveying of coarse grains through a very-narrow elbow. Powder Technol. 395, 811–821. https://doi.org/10.1016/j.powtec.2021.10.022.
Shen, Z., Wang, G., Huang, D., Jin, F., 2022. A resolved CFD-DEM coupling model for modeling two-phase fluids interaction with irregularly shaped particles. J. Comput. Phys. 448, 110695. https://doi.org/10.1016/j.jcp.2021.110695.
Tan, X., Weng, X., Ahmed, T.K., Bukovac, T., Enkababian, P., 2018. An improved ball sealer model for well stimulation. In: SPE International Conference and Exhibition on Formation Damage Control. https://doi.org/10.2118/189573-MS.
Wang, D., Wang, X., Liu, G., Economides, M.J., 2012. A new way of staged fracturing using ball sealers. SPE Prod. Oper. 27 (3), 278–283. https://doi.org/10.2118/

140529-PA.
Wang, Z., Liu, M., 2020. Semi-resolved CFD–DEM for thermal particulate flows with applications to fluidized beds. Int. J. Heat Mass Tran. 159, 120150. https://doi.org/10.1016/j.ijheatmasstransfer.2020.120150.
Washino, K., Chan, E.L., Tsujimoto, T., Tsuji, T., Tanaka, T., 2023. Development of resolved CFD–DEM coupling model for three-phase flows with non-spherical particles. Chem. Eng. Sci. 267, 118335. https://doi.org/10.1016/j.ces.2022.118335.
Xiong, H., Chen, Y., Chen, M., et al., 2021. Resolved CFD–DEM simulation on hydrodynamic bridging in a bend rectangle channel. J. Braz. Soc. Mech. Sci. Eng. 43 (7). https://doi.org/10.1007/s40430-021-03065-7.
Yamashiro, B.D., Tomac, I., 2022. Fracture roughness effects on slickwater proppant slurry settling attenuation. Powder Technol. 395, 516–533. https://doi.org/10.1016/j.powtec.2021.10.002.
Yuan, L., Zhou, F., Li, M., Wang, B., Bai, J., 2021. Experimental and numerical investigation on particle diverters transport during hydraulic fracturing. J. Nat. Gas Sci. Eng. 96. https://doi.org/10.1016/j.jngse.2021.104290.
Yuan, L., Zhou, F., Li, M., et al., 2022. Experimental study on diverter transport through perforations in multicluster fracturing of horizontal well. SPE J. 27 (2), 971–985. https://doi.org/10.2118/SPE-208606-PA.